Real-time instanton approach to quantum activation

Chang-Woo Lee,[1,*] Paul Brookes,[2,*] Kee-Su Park,[3] Marzena H. Szymańska,[2] and Eran Ginossar[4]
[1]*School of Computational Sciences, Korea Institute for Advanced Study, 85 Hoegi-ro, Dongdaemun-gu, Seoul 02455, South Korea*
[2]*Department of Physics and Astronomy, University College London, Gower Street, London WC1E 6BT, United Kingdom*
[3]*Department of Physics, Sungkyunkwan University, Suwon 16419, South Korea*
[4]*School of Mathematics and Physics, University of Surrey, Guildford GU2 7XH, United Kingdom*

(Received 20 November 2024; accepted 17 June 2025; published 17 July 2025)

Driven-dissipative nonlinear systems exhibit rich critical behavior, related to bifurcation, bistability, and switching, which underlie key phenomena in areas ranging from physics, chemistry, and biology [T. Wilhelm, BMC Syst. Biol. **3**, 90 (2009)] to social sciences and economics. The importance of rare fluctuations leading to a dramatic jump between two very distinct states, such as survival and extinction in population dynamics [A. Taitelbaum *et al.*, Phys. Rev. Lett. **125**, 048105 (2020); A. Kamenev and B. Meerson, Phys. Rev. E **77**, 061107 (2008)], success and bankruptcy in economics [S. Ghashghaie *et al.*, Nature (London) **381**, 767 (1996)], and the occurrence of earthquakes [L. Knopoff and Y. Kagan, J. Geophys. Res. **82**, 5647 (1977)] or of epileptic seizures [K. Lehnertz, *Extreme Events in Nature and Society* (Springer, Berlin, Heidelberg, 2006), pp. 123–143], have been already established. In the quantum domain, switching is of importance in both chemical reactions and the devices used in quantum state detection and amplification [R. Vijay *et al.*, Rev. Sci. Instrum. **80**, 111101 (2009)]. In particular, the simplest driven single oscillator model serves as an insightful starting point. Here we describe switching induced by quantum fluctuations and illustrate that an instanton approach within Keldysh field theory can provide a deep insight into such phenomena. We provide a practical recipe to compute the switching rates semi-analytically, which agrees remarkably well with exact solutions across a wide domain of drive amplitudes spanning many orders of magnitude. Being set up in the framework of Keldysh coherent states path integrals, our approach opens the possibility of studying quantum activation in many-body systems where other approaches are inapplicable.

DOI: 10.1103/5jtm-ht4n

I. INTRODUCTION

Quantum activation is a process in which a driven system, such as a nonlinear oscillator, switches between two metastable states of forced vibrations due to random noise from spontaneous emission events [1–9]. Since energy is continually pumped into the system, these switching events can occur even when the temperature of the bath is zero, unlike the process of classical activation. Although the system may spend the majority of its time close to metastable states, emission events may cause rare fluctuations, taking the system away from one metastable steady state towards an intermediate unstable state, and then into the basin of attraction of the other metastable state.

The instanton approach in quantum field theory has already been used to study qubit decoherence via quantum activation [10] for evaluating the decay time of metastable states [11] and switching rates [10,12], and existing theory can also explain some universal dependencies for switching of a single oscillator close to the bifurcation points in the semiclassical regime [13,14]. However, significant recent advances in superconducting, electromechanical, and optomechanical devices running beyond this regime necessitate a general approach [15,16].

The method for calculating switching which we now explore is based on Keldysh field theory [17–20]. Whereas in thermal equilibrium we can obtain switching rates by studying the dynamics of a system in imaginary time [21–24], this is no longer possible when drive and dissipation are included. In this situation the state of the system is described by a density matrix and in the formalism of Keldysh field theory this leads to a doubling of the dimensions of the phase space. The additional dimensions open paths for dissipative (noise-based) motion, see Fig. 1, to be included in the mean-field description of the dynamics and allow us to gain more insight into the processes of activation and switching. With this approach we can semi-analytically calculate the exponential dependence of the switching times on the drive amplitude and frequency and find that they agree with numerical simulations over a wide range of parameters. In particular, we find our method to work well when the nonlinearity of the oscillator is of a similar order as the oscillator decay rate, i.e., outside the semiclassical regime. Importantly, our results extend previous work to parameter ranges further away from the bifurcation points. This includes comprehensive numerical simulations and detailed comparison of the instanton-based results with the results of exact simulations of the Liouvillian master equation. Below we first describe our analytical approach based on Keldysh field theory, which is general and could be applied in a wide range of scenarios, even including many-particle systems. Later, we discuss numerical studies of the

[*]These authors contributed equally to this work.

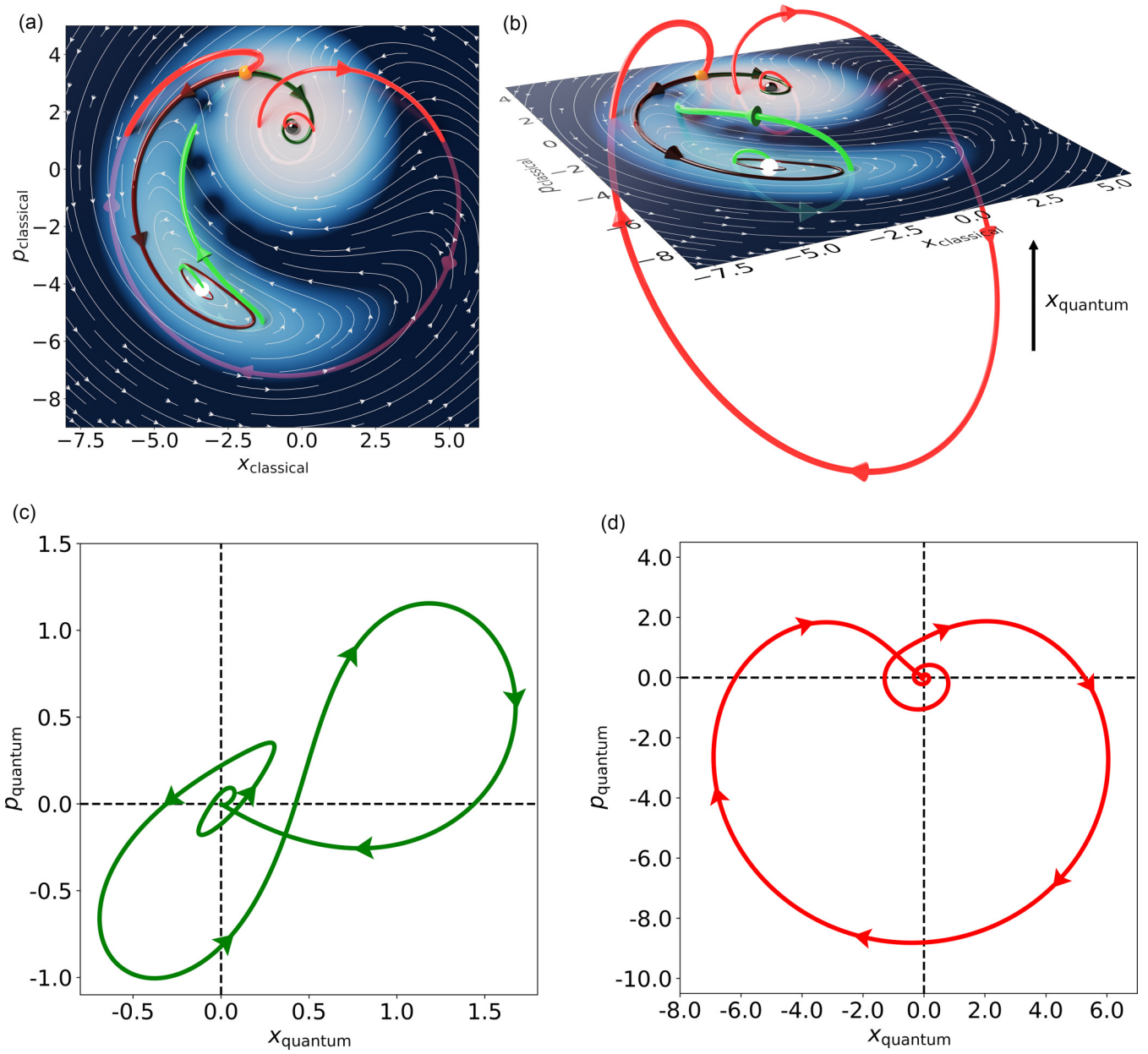

FIG. 1. Keldysh escape paths. The switching paths following the equations of motion derived using Keldysh field theory. The parameters of the model are $(\chi/\kappa, \delta/\kappa, \epsilon/\kappa) = (-0.5, 5.8, -4.0)$. The full four-dimensional path cannot be shown, so in panels (a) (top view) and (b) (angled view) we plot the two classical variables $x_{\text{classical}}$ and $p_{\text{classical}}$ as well as the quantum variable x_{quantum}. Within the classical plane defined by $x_{\text{quantum}} = p_{\text{quantum}} = 0$ we display a density plot of the Wigner function of the steady state along with the fixed points (white, black and yellow) of the classical equations of motion. The white and black balls mark the bright and dim fixed points, respectively, while the yellow ball marks the unstable point. The switching paths originate at the stable fixed points and immediately leave the classical plane. By utilizing the quantum degrees of freedom, the system is able to escape the classical basin of attraction of the bright state and arrive at the unstable point, from which it may relax classically to the other stable point. The quantum components x_{quantum} and p_{quantum} of the escape paths from (c) the bright state and (d) the dim state start and end at the values of zero, indicating that the escape path starts and ends in the classical plane.

Lindblad master equation, which we use to validate our analytical results.

II. DYNAMICS OF THE KERR OSCILLATOR

A. Keldysh action

We focus on the prototypical model of the nonlinear driven-dissipative Kerr oscillator in the quantum regime. The self-Kerr effect is a nonlinear shifting of a resonator frequency as a function of the number of photons in the mode. A simple quantum system where this can been seen is the quantum Duffing oscillator, with its term proportional to $(a^\dagger a)^2$ in the Hamiltonian, where a is the photon annihilation operator for a resonator mode. In the classical limit, this becomes the quadratic dependence of the refractive index on the electric-field strength, sometimes known as self-phase modulation [25–27]. This effect manifests itself at second order in a series expansion of the Jaynes–Cummings interaction in the

dispersive limit [15,28–30]. In a frame rotating at the drive frequency the Kerr oscillator Hamiltonian reads

$$H = \delta a^\dagger a + \chi a^\dagger a^\dagger a a + i\epsilon(a^\dagger - a), \tag{1}$$

where δ is the detuning between the oscillator and the drive frequency, χ is the nonlinearity of the oscillator, ϵ is the drive amplitude, and we have taken $\hbar = 1$. The rotating wave approximation has been applied.

All correlation functions and observables of this system, such as the rate of switching between metastable states, can be obtained from the partition function [18,20]

$$\mathcal{Z} = \int \mathcal{D}a_- \mathcal{D}a_-^* \mathcal{D}a_+ \mathcal{D}a_+^* e^{iS[a_+, a_+^*, a_-, a_-^*]}, \tag{2}$$

which in the Keldysh formalism involves a path integral over two degrees of freedom: the forward a_+ and backward a_- time paths. The action S is given by

$$S = \int L dt, \tag{3}$$

$$\begin{aligned} L = {} & a_+^* i\partial_t a_+ - a_-^* i\partial_t a_- + i\varepsilon(a_+^* - a_+ - a_-^* + a_-) \\ & - \delta(a_+^* a_+ - a_-^* a_-) - \chi(a_+^{*2} a_+^2 - a_-^{*2} a_-^2) \\ & - i\kappa(2a_+ a_-^* - a_+^* a_+ - a_-^* a_-), \end{aligned} \tag{4}$$

where $+$ $(-)$ denotes the fields in forward (backward) branches. The dissipative terms have been obtained from integration over the degrees of freedom of a bosonic bath coupled to the system [31]. In the present case we consider a Markovian bath at zero temperature in order to compare with numerical results obtained for a Lindblad master equation.

B. Switching paths

We can now define classical and quantum field variables according to $a_c = (a_+ + a_-)/\sqrt{2}$, $a_q = (a_+ - a_-)/\sqrt{2}$. In the absence of quantum fluctuations, the evolution will be restricted to the classical plane (i.e., $a_q = 0$) for the system to move towards either of two stable fixed points, corresponding to the bright and dim metastable states. Activation and tunneling events which allow switching from one metastable state to another are expected to occur via the quantum degree of freedom a_q.

To study the dynamics of our quantum and classical field variables we now decompose them into real and imaginary components according to

$$a_c = (x_c + ip_c)/\sqrt{2}, \quad a_q = (\tilde{x}_q + i\tilde{p}_q)/\sqrt{2}. \tag{5}$$

In these terms the Lagrangian reads

$$\begin{aligned} L = {} & \dot{x}_c \tilde{p}_q - \dot{p}_c \tilde{x}_q - \left[\delta + \frac{\chi}{2}\left(x_c^2 + p_c^2 + \tilde{x}_q^2 + \tilde{p}_q^2\right)\right] \\ & \times (x_c \tilde{x}_q + p_c \tilde{p}_q) + \kappa(x_c \tilde{p}_q - p_c \tilde{x}_q) \\ & + i\kappa\left(\tilde{x}_q^2 + \tilde{p}_q^2\right) + 2\varepsilon \tilde{p}_q, \end{aligned} \tag{6}$$

up to total derivatives, while the partition function is now expressed as

$$\mathcal{Z} = \int \mathcal{D}x_c \mathcal{D}p_c \mathcal{D}\tilde{x}_q \mathcal{D}\tilde{p}_q e^{iS[x_c, p_c, \tilde{x}_q, \tilde{p}_q]}. \tag{7}$$

We may wish to approximate the above Lagrangian by taking into account only the saddle-point (the most probable) paths. This would allow us to determine the equations of motion and find the paths which connect the metastable states, and which dominate the partition function. Unfortunately, no such paths exist for real values of the coordinates (see Appendix A). Motion is constrained to the classical plane and there are no paths leaving the metastable states.

At this point we can consider the approach explored in Ref. [18]: what if the stationary paths lie along the imaginary axes of $\tilde{x}_q$ and $\tilde{p}_q$ instead? Although the integrals in Eq. (7) are all along real axes we may use Cauchy's theorem to deform the paths without changing their values. Therefore we choose to make the quantum coordinates imaginary and we rewrite them as follows:

$$\tilde{x}_q \to -ip_q, \quad \tilde{p}_q \to ix_q \tag{8}$$

in terms of which the Lagrangian can be written as

$$iL = -[\dot{x}_c p_c + \dot{p}_c p_q - H(x_c, p_c, x_q, p_q)], \tag{9}$$

with an auxiliary Hamiltonian given by

$$\begin{aligned} H = {} & \left(\delta + \frac{\chi}{2}\left(x_c^2 + p_c^2 - x_q^2 - p_q^2\right)\right)(p_c x_q - x_c p_q) \\ & - \kappa(x_c x_q + p_c p_q) + \kappa\left(x_q^2 + p_q^2\right) + 2\varepsilon x_q. \end{aligned} \tag{10}$$

The saddle-point equations of motion are then given by

$$\dot{z}_c = \partial_{z_q} H, \quad \dot{z}_q = -\partial_{z_c} H, \tag{11}$$

where $z_c = (x_c, p_c)$ and $z_q = (x_q, p_q)$ and the action, consequently, becomes $iS = i\int L\, dt = -\int dz_c \cdot z_q$. We see that our equations of motion now allow evolution out of the classical plane and can connect the metastable states, as seen in Fig. 1.

To identify the fixed points corresponding to these metastable states we obtain the classical equations of motion by setting the quantum variables to zero, $x_q = p_q = 0$. It is known that in the bistable regime there are three fixed points within this plane, two of which are stable. We refer to these as the bright and dim states according to the intensity of the oscillator field at those points. Meanwhile, there is a third unstable point lying on the separatrix which divides the plane into the two basins of attraction of the stables states.

Although the bright and dim states are stable within the classical plane, we find that quantum fluctuations can allow rare escape events, during which the system moves to the unstable point along a path lying outside the plane, where quantum components of the fields are nonzero. Once it has reached the unstable point it may relax along the classical path to the other stable point. The trajectories of these escape events are described by the full equations of motion above and examples are displayed in Fig. 1.

Here we are particularly interested in calculating the rate at which these escape events occur. In the saddle-point approximation, the rate of switching from the point $\boldsymbol{Z}_j$ to the other stable point $\boldsymbol{Z}_k$ can be written as

$$\gamma_{j\to k} = \omega_{j\to u} e^{iS_{j\to u}}, \tag{12}$$

where the prefactor $\omega_{j\to u}$ is the attempt frequency [11,32] and the action is calculated by integrating the Lagrangian along the path from $\boldsymbol{Z}_j$ to the unstable point $\boldsymbol{Z}_u$. Results from these

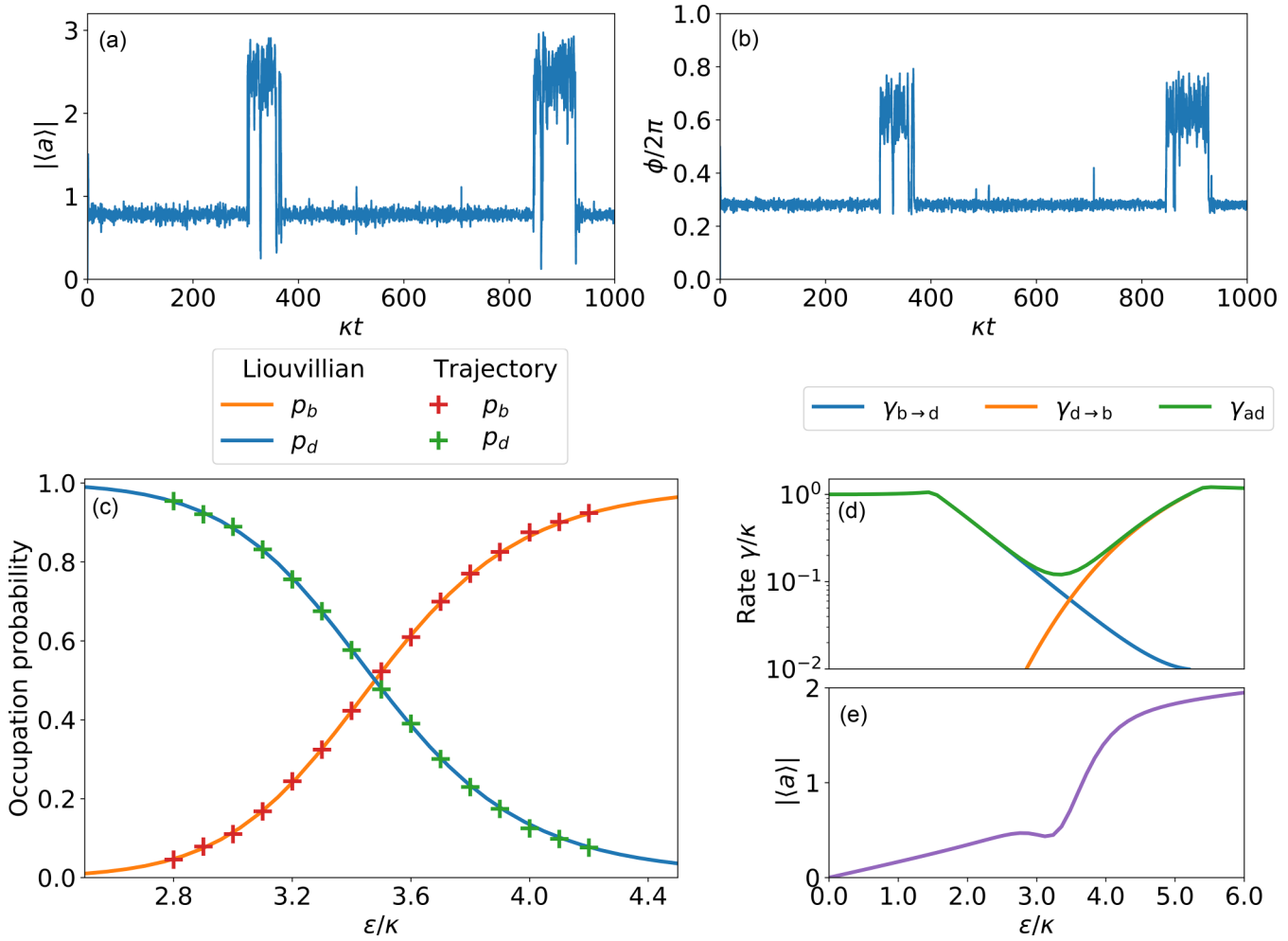

FIG. 2. Results of Liouvillian and stochastic Schrödinger equation methods. (a) The amplitude and (b) the phase of the cavity state during a quantum trajectory produced at $(\chi/\kappa, \delta/\kappa, \epsilon/\kappa) = (-0.5, 5.8, 4.0)$. In panel (a) the amplitude goes up to ≈ 3, corresponding to an occupation of ≈ 9 photons, allowing for accurate simulations in a small truncated Hilbert space. In the bistable regime this trajectory displays sudden jumps between two metastable states whose lifetimes are typically much longer than the lifetime of the cavity $1/\kappa$. (c) The occupation probabilities of the bright and dim states vs the drive amplitude ϵ, obtained by studying the eigenstates of the Liouvillian at $(\chi/\kappa, \delta/\kappa) = (-1.0, 6.0)$. As the system moves through the bistable regime it transitions from a state consisting entirely of the dim state to entirely of the bright state. The markers indicate occupation probabilities calculated by studying the trajectories produced using a stochastic Schrödinger equation. Excellent agreement between these methods is seen. (d) The asymptotic decay rate (green) falls significantly in the bistable regime, indicating the onset of critical slowing down. The bright (blue) and dim (orange) state occupation probabilities used to calculate the switching rates. (e) The transmission of the cavity as we increase the drive. The oscillator amplitude reaches ≈ 2, corresponding to an occupation of ≈ 4 photons. The bistable regime coincides with a small dip before a sudden increase in the cavity amplitude.

calculations can be seen in Figs. 3(b) and 3(c). Details of the calculations can be found in Appendix B.

C. Master equation and stochastic Schrödinger equation

Before we discuss these results, we also wish to obtain some exact numerical results via an alternative approach as verification. Assuming the dilute-gas limit of instantons [11] and an effective two-state model [32,33], the occupation probabilities of the bright and dim states are governed by the following rate equation:

$$\frac{d}{dt}\begin{pmatrix} p_{\rm b} \\ p_{\rm d} \end{pmatrix} = \begin{pmatrix} -\gamma_{\rm b\to d} & \gamma_{\rm d\to b} \\ \gamma_{\rm b\to d} & -\gamma_{\rm d\to b} \end{pmatrix}\begin{pmatrix} p_{\rm b} \\ p_{\rm d} \end{pmatrix}. \tag{13}$$

At long times the system relaxes to a steady state in which the probabilities are given by

$$p^{ss}_{\rm b(d)} = \gamma_{\rm d(b)\to b(d)}/\gamma_{\rm total}, \quad \gamma_{\rm total} \equiv \gamma_{\rm b\to d} + \gamma_{\rm d\to b}. \tag{14}$$

The steady-state occupation probabilities $p^{ss}_{\rm b(d)}$ and the total decay rate $\gamma_{\rm total}$ can both be obtained by studying the dynamics of the Liouvillian master equation. This is outlined in Appendix C, where we find the eigenvalues and eigenvectors of the Liouvillian matrix and highlight the equality between $\gamma_{\rm total}$ and the asymptotic decay rate $\gamma_{\rm ad}$, which is the real component of the slowest decaying perturbation from the steady state. This quantity is plotted in Figs. 2(c) and 2(d). Consequently, we are able to obtain the switching rates according to

$$\gamma_{\rm d(b)\to b(d)} = p_{\rm b(d)}\gamma_{\rm ad}. \tag{15}$$

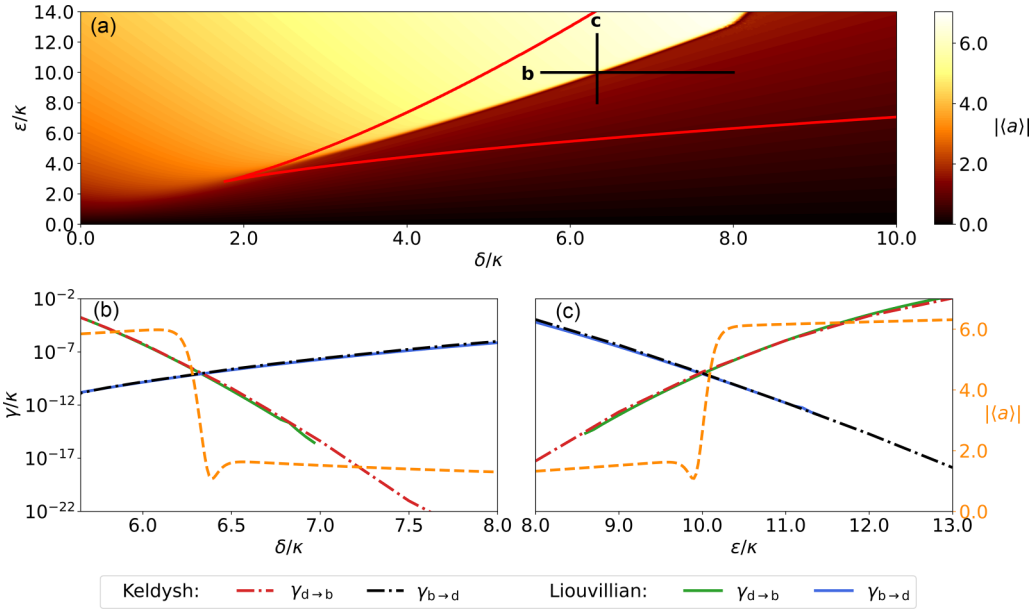

FIG. 3. Comparing Keldysh and Liouvillian switching rates at $\chi/\kappa = -0.1$. (a) The oscillator amplitude as a function of δ and ϵ. The boundaries of the bistable region (red solid lines) surround a sudden transition from low to high amplitude states as the drive (detuning) is increased (decreased) and are calculated using the classical equations of motion. In panels (b) (for $\epsilon/\kappa = 10.0$) and (c) (for $\delta/\kappa = 6.33$) we plot the switching rates and oscillator amplitude along the black lines marked in panel (a). The oscillator amplitude reaches ≈6, corresponding to an occupation of ≈36 photons, placing the system in the regime where the instanton approach is most applicable and direct comparison with QUTIP becomes challenging. Here, we have fitted $\omega_{b\to d}/\kappa = 1.0$ and $\omega_{d\to b}/\kappa = 0.1$ to give an excellent agreement between the Keldysh and Liouvillian switching rates over several orders of magnitude. This indicates that our assumption that the attempt rates vary slowly with the drive parameters was remarkably accurate and the dominant variations in the switching rates are well described by the action of the optimal switching path. The overlaid cavity amplitude (orange) shows that the crossing of the rates coincides with transition between high- and low-amplitude states of the oscillator.

In this manner we can calculate the switching rates in the bistable regime, which are also included in Fig. 2(d).

Next, we also obtain switching rates more directly by observing switching events in solutions of the stochastic Schrödinger equation for an optical cavity under heterodyne detection [34]. These simulations were performed using the stochastic solvers available in the Quantum Toolbox in Python (QUTIP) [35]. By simulating a trajectory over a sufficiently long period of time, we are able to observe many switching events [Figs. 2(a) and 2(b)] and obtain the occupation probabilities displayed in Fig. 2(c), which agree closely with the results of the master equation.

D. Keldysh switching rates

We can now move forward and compare our various methods in Fig. 3, using the master equations predictions as a validation for the path integral method. In Fig. 3(a) we first plot the steady-state oscillator amplitude as a function of δ and ϵ at $\chi/\kappa = -0.1$. The boundaries of the bistable regime according to the classical equations of motion are marked in red and we see the familiar opening of this regime in the upper-right quadrant. Within this regime, we also see the expected sudden transition between low- and high-amplitude states of the oscillator. These states are separated by a small dip in intensity due to destructive interference between the bistable states, visible in Figs. 3(b) and 3(c).

The black lines in Fig. 3(a) highlight the parameter ranges over which Figs. 3(b) and 3(c) were produced. In these ranges we calculated the paths escaping from the metastable states to the unstable state, along with their actions, in order to obtain the switching rates in Eq. (12). Since we currently do not have a means to calculate the attempt frequencies $\omega_{b\to u}$ and $\omega_{d\to u}$, we use them as fitting parameters and assume they vary little with changes in δ or κ. Despite this we are able to obtain excellent agreement between the switching rates produced by the Keldysh and Liouvillian methods over several orders of magnitude. This indicates that the exponential dependence on the action is by far the dominant factor governing the switching rates and that it can be accurately calculated using the Keldysh method.

Finally, we explore how the switching rates vary with the rate of dissipation κ. Previous approaches to calculating switching rates have been limited either to the weak-dissipation limit [1,2,36], or close to the bifurcation points [13]. In particular, Ref. [1] showcased an approach that involved deriving the equation for the density matrix and applying saddle-point methods to obtain four-dimensional equations of motion similar to those obtained from the Keldysh formalism in Eq. (11). However, these equations were only solved in the zero-damping limit, which we now extend beyond.

In later work, the switching dynamics were studied in great detail in the vicinity of the bifurcation points [13,14]. In this regime, the unstable state can be found very close to either of the metastable states and, as these two states approach each other in phase space, a soft mode emerges between them along which the evolution of the system slows down. The

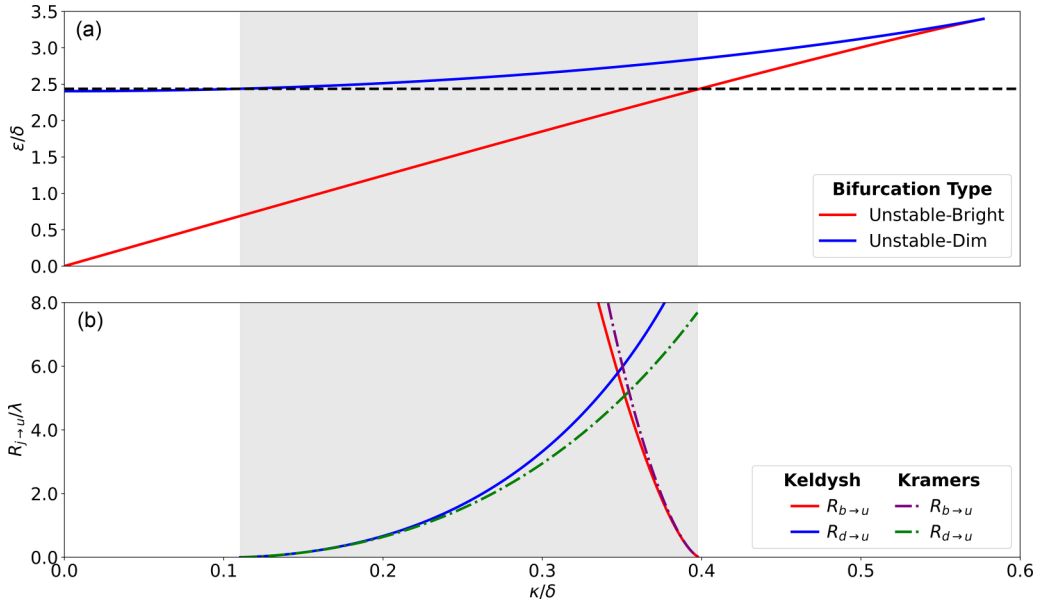

FIG. 4. Measuring the activation barrier height at $\chi/\delta = -1/78$. (a) The limits of the bistable regime as a function of κ and ϵ. As we increase the drive amplitude the bistable regime appears when the bright and unstable states emerge at the unstable-bright bifurcation. When there is no damping present in the system this bifurcation happens at zero drive. For sufficiently high drive amplitudes the unstable and dim states combine and annihilate each other at the unstable-dim bifurcation. In panel (b) we plot the variation of the barrier height $R_{j\to u}$ with κ at $\epsilon/\delta = 2.44$. This barrier height is measured relative to the scaled Planck constant $\lambda = 0.0128$. The barrier height is calculated in two ways: First, we solve the equations of motion derived from the Keldysh approach and calculate the actions along the paths escaping from the metastable states to the unstable state. These barrier heights are marked by solid lines. Second, we treat escape as a Kramers problem in a one-dimensional potential close to the bifurcation points. These results are marked by dashed lines. Both approaches agree close to the bifurcation points where the one-dimensional approximation can be made but begin to disagree in the middle of the bistable regime. Since the switching rates depend exponentially upon the barrier height this can lead to significant disagreements in calculated switching rates, especially at the crossing point where both switching rates and their corresponding populations are equal.

system becomes effectively one dimensional and the dynamics resemble a Kramers problem in which fluctuations may allow the system to escape from the metastable state by climbing a potential barrier whose peak is found at the unstable state. Beyond this point the system then decays to the other metastable state and the switching event is complete. This approach proved successful and was able to accurately model the switching rates, but only in the vicinity of the bifurcation points where this soft mode emerges. The switching rate is primarily determined by the quantum activation energy R_A, whose scaling behavior near the bifurcation points was calculated to be $R_A \propto |\eta|^{3/2}$ for a resonantly driven Kerr oscillator [13], where η is the distance from the saddle-node bifurcation (see Appendix D).

In Fig. 4 we compare the Kramers problem approach with the results of the Keldysh approach. In the Kramers approach the switching rates can be modeled in terms of a barrier height $R_{j\to u}$ as

$$\gamma_{j\to k} \propto \exp(-R_{j\to u}/\lambda). \tag{16}$$

In this equation $R_{j\to u}$ represents the barrier height to move from metastable state j to the unstable point u. It is rescaled by the scaled Planck constant $\lambda = \chi/\delta$. In terms of the switching actions we have studied so far, this barrier height is given by $R_{j\to u} = i\lambda S_{j\to u}$. Both the Kramers and Keldysh approaches agree in the vicinity of the bifurcation points where the escape problem becomes one dimensional. The barrier starts at zero at these bifurcation points and increases as we move into the bistable regime. Both the Kramers and Keldysh approaches show a monotonic dependence on *kappa* but disagree quantitatively towards the middle of the bistable regime where the rates are balanced.

III. CONCLUSION

In conclusion, we have shown that the Keldysh technique can be used to obtain an extended mean-field theory, which captures the quantum activation and switching dynamics in a Kerr oscillator. By assuming that the system predominantly follows the saddle-point path of the Keldysh action we are able to predict switching rates which are in excellent agreement with numerical simulations of the exact dynamics and we explain how the system moves in the extended classical-quantum phase space between the different fixed points.

The potential of our method goes beyond this demonstration. In this work we chose to highlight the power of the Keldysh approach when applied to a system in contact with a Markovian thermal bath, which allowed us to cross-check our results against those obtained using a standard Liouvillian master equation. However, in the future it could be possible to take memory effects into account by, for example, allowing κ in Eq. (4) to vary as a function of frequency [31].

Furthermore, since the Keldysh approach is formulated in the language of second quantization (i.e., coherent-state path integrals), it can be straightforwardly applied to more complex many-body systems such as coupled oscillators, spins coupled

to bosons, or even bosonic lattices. Although methods already exist which can produce similar results for the Kerr oscillator, it would not be straightforward to apply them to more complex systems. For example, an alternative approach to the calculation of switching rates has previously been explored based on applying saddle-point methods to the evolution of the Wigner function [1]. As in our Keldysh method, this approach relies on calculating the action along a path escaping from the basin of attraction via the unstable point. In the limit of weak nonlinearity the equations of motion converge; however, that method would only be applicable to a single particle and it would be challenging to extend to non-Markovian dynamics. This generalizability is a key advantage of the Keldysh approach and will be the main theme of future work as we go beyond regimes which can easily be compared with other methods.

ACKNOWLEDGMENTS

C.-W.L. acknowledges support by National Research Foundation of Korea (Grant no. NRF-2017R1D1A1B04032142). M.H.S. acknowledges support from EPSRC Grants No. EP/S019669/1, No. EP/R04399X/1, No. EP/V026496/1 (Quantera InterPol), EP/K003623/2. E.G. acknowledges support from EPSRC Grant EP/T001062/1.

DATA AVAILABILITY

The data that support the findings of this study are openly available in "github" at [37].

APPENDIX A: EQUATIONS OF MOTION

In terms of field quadratures the Lagrangian is given by

$$\begin{aligned} L = {} & \dot{x}_c\tilde{p}_q - \dot{p}_c\tilde{x}_q + \kappa(x_c\tilde{p}_q - p_c\tilde{x}_q) \\ & - \left[\delta + \frac{\chi}{2}\left(x_c^2 + p_c^2 + \tilde{x}_q^2 + \tilde{p}_q^2\right)\right](x_c\tilde{x}_q + p_c\tilde{p}_q) \\ & + i\kappa\left(\tilde{x}_q^2 + \tilde{p}_q^2\right) + 2\varepsilon\tilde{p}_q, \end{aligned} \tag{A1}$$

while the partition function is given by

$$\mathcal{Z} = \int \mathcal{D}x_c\mathcal{D}p_c\mathcal{D}\tilde{x}_q\mathcal{D}\tilde{p}_q e^{iS[x_c,p_c,\tilde{x}_q,\tilde{p}_q]}. \tag{A2}$$

We may wish to estimate this partition function using a saddle-point approximation. In this method we find the dominant path in the integral above by solving the Euler-Lagrange equations for the Lagrangian above. These equations of motion are given by

$$\begin{aligned} \partial_t x_c = {} & \delta p_c - 2\epsilon - 2i\kappa\tilde{p}_q - \kappa x_c \\ & + \tfrac{1}{2}\chi\left(p_c^3 + 3p_c\tilde{p}_q^2 + p_c x_c^2 + p_c\tilde{x}_q^2 + 2\tilde{p}_q x_c\tilde{x}_q\right), \end{aligned} \tag{A3}$$

$$\begin{aligned} \partial_t p_c = {} & -\delta x_c - \kappa(p_c - 2i\tilde{x}_q) \\ & - \tfrac{1}{2}\chi\left(p_c^2 x_c + 2p_c\tilde{p}_q\tilde{x}_q + \tilde{p}_q^2 x_c + x_c^3 + 3x_c\tilde{x}_q^2\right), \end{aligned} \tag{A4}$$

$$\begin{aligned} \partial_t \tilde{x}_q = {} & \tfrac{1}{2}\chi\left(3p_c^2\tilde{p}_q + 2p_c x_c\tilde{x}_q + \tilde{p}_q^3 + \tilde{p}_q x_c^2 + \tilde{p}_q\tilde{x}_q^2\right) \\ & + \delta\tilde{p}_q + \kappa\tilde{x}_q, \end{aligned} \tag{A5}$$

$$\begin{aligned} \partial_t \tilde{p}_q = {} & -\tfrac{1}{2}\chi\left(p_c^2\tilde{x}_q + 2p_c\tilde{p}_q x_c + \tilde{p}_q^2\tilde{x}_q + 3x_c^2\tilde{x}_q + \tilde{x}_q^3\right) \\ & - \delta\tilde{x}_q + \kappa\tilde{p}_q. \end{aligned} \tag{A6}$$

If we examine these equations carefully it becomes clear that there are no solutions for purely real values of x_c, p_c, $\tilde{p}_q$, and $\tilde{p}_q$. If all coordinates are initialized to real values then x_c and p_c will immediately evolve to complex values. However, we may be able to find solutions where x_c and p_c are both real while $\tilde{p}_q$ and $\tilde{p}_q$ are purely imaginary.

This may seem problematic since the path integrals in the partition function above are over real values of $\tilde{p}_q$ and $\tilde{p}_q$. However, we can use Cauchy's theorem to deform the contours of integration to follow the imaginary axes without changing the values of the integrals [18]. To account for this we find it convenient to rewrite the equations of motion using

$$\tilde{x}_q \to -ip_q, \quad \tilde{p}_q \to ix_q. \tag{A7}$$

In terms of these real coordinates we find

$$\begin{aligned} \partial_t x_c = {} & \delta p_c - 2\epsilon + 2\kappa x_q - \kappa x_c \\ & + \tfrac{1}{2}\chi\left(p_c^3 - 3p_c x_q^2 + p_c x_c^2 - p_c p_q^2 + 2x_q x_c p_q\right), \end{aligned} \tag{A8}$$

$$\begin{aligned} \partial_t p_c = {} & -\delta x_c - \kappa(p_c - 2p_q) \\ & - \tfrac{1}{2}\chi\left(p_c^2 x_c + 2p_c x_q p_q - x_q^2 x_c + x_c^3 - 3x_c p_q^2\right), \end{aligned} \tag{A9}$$

$$\begin{aligned} \partial_t x_q = {} & \tfrac{1}{2}\chi\left(p_q p_c^2 - p_q^3 + 3p_q x_c^2 - p_q x_q^2 - x_c p_c x_q\right) \\ & + \delta p_q + \kappa x_q, \end{aligned} \tag{A10}$$

$$\begin{aligned} \partial_t p_q = {} & \tfrac{1}{2}\chi\left(2p_q p_c x_c + x_q p_q^2 + x_q^3 - x_q x_c^2 - 3p_c^2 x_q\right) \\ & - \delta x_q + \kappa p_q. \end{aligned} \tag{A11}$$

The solution to the above equations of motion can be used in the saddle-point approximation of the partition function. For cases where κ becomes frequency dependent, e.g., at finite temperature, the action will be nonlocal in time and the saddle-point equations will become a set of coupled integro-differential equations.

APPENDIX B: OBTAINING SWITCHING PATHS

1. Classical fixed points

The equations of motion (11) have three fixed points within the classical plane, two of which are stable while the other is unstable. The dim and bright fixed points are denoted by $\boldsymbol{Z}_d$ and $\boldsymbol{Z}_b$, respectively, and the unstable point is denoted $\boldsymbol{Z}_u$. The two stable points each have their own basin of attraction and the unstable point lies on the boundary which separates these two basins.

To switch from one stable point to another the system must leave the classical plane by utilizing the quantum dimensions x_q and p_q. The path of least action takes the system to the unstable point, from which it may move into the basin of attraction of the other stable point.

2. Stability analysis

To classify the fixed points and understand the escape mechanisms, we perform a comprehensive stability analysis

by linearizing the full four-dimensional equations of motion around each fixed point.

To linearize the equations of motion, we write the state of the system as

$$\mathbf{Z}(t) = \mathbf{Z}_0 + \Delta\mathbf{Z}(t), \tag{B1}$$

where

$$\mathbf{Z}_0 = (x_{c0}, p_{c0}, x_{q0}, p_{q0}) \tag{B2}$$

denotes the coordinates of a fixed point, and $\Delta\mathbf{Z}(t)$ represents a small deviation from that point. Expanding the equations of motion to first order in $\Delta\mathbf{Z}(t)$ yields

$$\frac{d}{dt}\Delta\mathbf{Z}(t) = J(\mathbf{Z}_0)\Delta\mathbf{Z}(t), \tag{B3}$$

where $J(\mathbf{Z}_0)$ is the Jacobian matrix evaluated at $\mathbf{Z}_0$. The Jacobian matrix J, evaluated at a fixed point $\mathbf{Z}_0$, is given by

$$J(\mathbf{Z}_0)_{ij} = \left.\frac{\partial \dot{\mathbf{Z}}_i}{\partial \mathbf{Z}_j}\right|_{\mathbf{Z}=\mathbf{Z}_0}. \tag{B4}$$

The equations of motion can be written as

$$\dot{\mathbf{Z}} = (\dot{x}_c, \dot{p}_c, \dot{x}_q, \dot{p}_q) = \left(\frac{\partial H}{\partial x_q}, \frac{\partial H}{\partial p_q}, -\frac{\partial H}{\partial x_c}, -\frac{\partial H}{\partial p_c}\right), \tag{B5}$$

and the explicit 4×4 Jacobian matrix is

$$J(\mathbf{Z}_0) = \begin{pmatrix} \frac{\partial^2 H}{\partial x_q \partial x_c} & \frac{\partial^2 H}{\partial x_q \partial p_c} & \frac{\partial^2 H}{\partial x_q^2} & \frac{\partial^2 H}{\partial x_q \partial p_q} \\ \frac{\partial^2 H}{\partial p_q \partial x_c} & \frac{\partial^2 H}{\partial p_q \partial p_c} & \frac{\partial^2 H}{\partial p_q \partial x_q} & \frac{\partial^2 H}{\partial p_q^2} \\ -\frac{\partial^2 H}{\partial x_c^2} & -\frac{\partial^2 H}{\partial x_c \partial p_c} & -\frac{\partial^2 H}{\partial x_c \partial x_q} & -\frac{\partial^2 H}{\partial x_c \partial p_q} \\ -\frac{\partial^2 H}{\partial p_c \partial x_c} & -\frac{\partial^2 H}{\partial p_c^2} & -\frac{\partial^2 H}{\partial p_c \partial x_q} & -\frac{\partial^2 H}{\partial p_c \partial p_q} \end{pmatrix}. \tag{B6}$$

The eigenvalues and eigenvectors of the Jacobian $J(\mathbf{Z}_0)$ provide the local stability properties of the fixed point. Specifically, consider the eigenvalue problem

$$J(\mathbf{Z}_0)\mathbf{v}_i = \lambda_i \mathbf{v}_i. \tag{B7}$$

Any small deviation from the fixed point can be expressed as a linear combination of these eigenvectors:

$$\Delta\mathbf{Z}(t) = \sum_{i=1}^{4} c_i \mathbf{v}_i e^{\lambda_i t}, \tag{B8}$$

where the coefficients c_i are determined by the initial condition $\Delta\mathbf{Z}(0) = \sum_{i=1}^{4} c_i \mathbf{v}_i$. This expansion illustrates how $\Delta\mathbf{Z}(t)$ evolves over time: each eigenmode evolves as $e^{\lambda t}$, where the real part of λ governs the exponential growth or decay. Specifically, eigenvalues with positive real parts lead to exponential growth of the corresponding perturbations, while those with negative real parts result in exponential decay. Moreover, if an eigenvalue is complex, its imaginary part will introduce oscillatory behavior on top of this exponential trend.

Because the full system is Hamiltonian with canonical coordinates for the classical and quantum fields, the Jacobian is a symplectic matrix satisfying

$$J^T \Omega J = \Omega, \quad \text{where} \quad \Omega = \begin{pmatrix} 0 & I_2 \\ -I_2 & 0 \end{pmatrix}, \tag{B9}$$

where I_2 is the 2×2 identity matrix. This symplectic structure leads to important constraints on the eigenvalue spectrum: if λ is an eigenvalue, then $-\lambda$ must also be an eigenvalue. Combined with complex-conjugate pairing, eigenvalues appear in quadruplets: λ, $-\lambda$, λ^*, and $-\lambda^*$.

The symplectic structure also implies a crucial biorthogonality relation between left and right eigenvectors. For any two distinct eigenvalues λ_i and λ_j, their corresponding eigenvectors satisfy

$$\mathbf{w}_i^T \Omega \mathbf{v}_j = 0 \quad \text{if} \quad \lambda_i \neq \lambda_j, \tag{B10}$$

where $\mathbf{w}_i$ and $\mathbf{v}_j$ are the left and right eigenvectors, respectively. This orthogonality relationship is essential for constructing escape trajectories because it determines which linear combinations of eigenmodes correspond to physically realizable paths in the four-dimensional phase space. Specifically, if $\mathbf{v}$ is a right eigenvector with eigenvalue λ, then $\Omega\mathbf{v}$ is a left eigenvector with eigenvalue $-\lambda$, which couples the classical stability (negative eigenvalues) with quantum instability (positive eigenvalues) and enables escape from classically stable states.

3. Fixed point classification

For the stable fixed points, the classical equations of motion (restricted to $x_q = p_q = 0$) are not Hamiltonian due to drive and dissipation. The stability behavior depends on the location within the bistable regime. The eigenvalues are given either by

$$\lambda \in \{-\kappa_1, -\kappa_2\} \tag{B11}$$

near a saddle-node bifurcation (nodes with different decay rates), where perturbations decay monotonically to the fixed point, or by

$$\lambda \in \{-\kappa - i\omega, -\kappa + i\omega\} \tag{B12}$$

deeper into the bistable regime (focus points with spiraling decay), where perturbations exhibit damped oscillations. This distinction between node and focus behavior has important implications for the computational feasibility of finding escape trajectories, as the spiraling motion can introduce widely different timescales that challenge numerical methods.

When we extend the analysis to include quantum fields, the system becomes Hamiltonian and we find two additional eigenvalues with positive real parts that complete the expected quadruplets:

$$\lambda \in \{-\kappa_1, -\kappa_2, \kappa_1, \kappa_2\} \tag{B13}$$

near bifurcations, or

$$\lambda \in \{-\kappa - i\omega, -\kappa + i\omega, \kappa - i\omega, \kappa + i\omega\} \tag{B14}$$

away from them. Crucially, the eigenvectors with positive eigenvalues provide escape paths from the classically stable points via quantum fluctuations. These unstable eigenvectors have components in both classical and quantum dimensions, illustrating how quantum fluctuations couple to classical motion to enable transitions that would be forbidden in a purely classical system. The coupling between classical stability (negative eigenvalues) and quantum instability (positive

eigenvalues) is the mechanism by which the system can escape from apparently stable states.

Meanwhile, at the saddle point in the classical case, the eigenvalues are

$$\lambda \in \{-\kappa_1, +\kappa_2\}, \tag{B15}$$

describing incoming and outgoing motion in the classical plane. When quantum fields are included, these pair with

$$\lambda \in \{-\kappa_1, +\kappa_2, +\kappa_1, -\kappa_2\}. \tag{B16}$$

The additional eigenvectors allow motion along directions in the full four-dimensional phase space and provide stable manifolds for escape trajectories to reach the saddle point.

4. Numerical implementation

The eigenvalue analysis reveals significant computational challenges for finding escape trajectories. At small decay rates deep in the bistable regime, stable fixed points exhibit strong oscillatory behavior with the ratio of imaginary to real parts of eigenvalues becoming very large. This causes escape trajectories to have significant spiraling motion with slow escape rates, where widely differing timescales and accumulation of numerical errors make it challenging to find exact paths from fixed points to the saddle point.

Near bifurcation points, one eigenvalue of the saddle point approaches zero, indicating emergence of a soft mode connecting the saddle to one of the stable fixed points. This simplifies the escape dynamics and corresponds to the one-dimensional Kramers problem, making trajectory computation more tractable.

The probability of a successful escape event is proportional to $e^{iS_{j\to u}}$, where $iS_{j\to u}$ is the action calculated along the path from stable fixed point j to the unstable point:

$$iS_{j\to u} = -\int_{\mathbf{z}_j\to\mathbf{z}_u} d\mathbf{z}_c \cdot \mathbf{z}_q. \tag{B17}$$

This action is computed from the numerical solution of the equations of motion.

The theoretical predictions for eigenvalue behavior can be verified numerically across parameter space. Using parameters $\chi/\kappa = -0.1$ and $\delta/\kappa = 7.8$, we plot the real and imaginary parts of the eigenvalues around each fixed-point type, along with the upper and lower bifurcation lines to clearly mark the limits of the bistable regime. Figures 5 and 6 show the eigenvalue spectra for the three types of fixed points in our system.

Key features observed include: (1) complex eigenvalues forming conjugate pairs across most of the parameter space for stable points, indicating oscillatory motion (focus behavior); (2) transition to purely real eigenvalues near bifurcation points, transforming fixed points into nodes; and (3) for the saddle point, eigenvalues maintain opposite signs throughout the bistable regime, with one pair approaching zero near bifurcations indicating soft-mode emergence.

The implications for trajectory computation are illustrated in Fig. 4, which shows classical decay trajectories from the saddle to the dim fixed point under different conditions. In the top-left panel we examine the system at small decay rate ($\kappa/\delta = 0.1/7.8, \epsilon/\delta = 10.0/7.8$) deep within the bistable regime, leading to a focus point with decaying spiralling motion. The small value of the decay rate causes the motion to be almost circular.

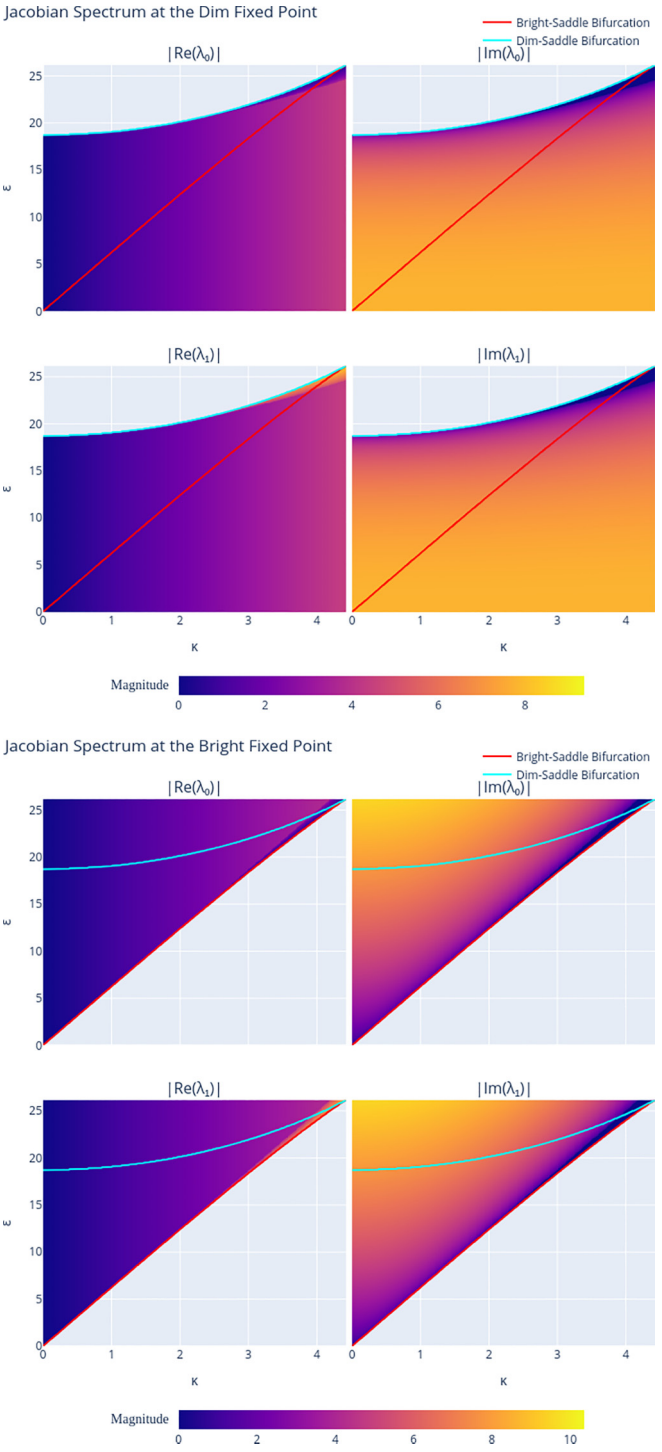

FIG. 5. Eigenvalue spectra of stable fixed points. Real and imaginary parts of eigenvalues for (top) dim fixed point and (bottom) bright fixed point across parameter space. Both show the characteristic transition from complex eigenvalues (focus behavior) in most regions to real eigenvalues (node behavior) near bifurcation boundaries, indicating the change from oscillatory to monotonic approach dynamics.

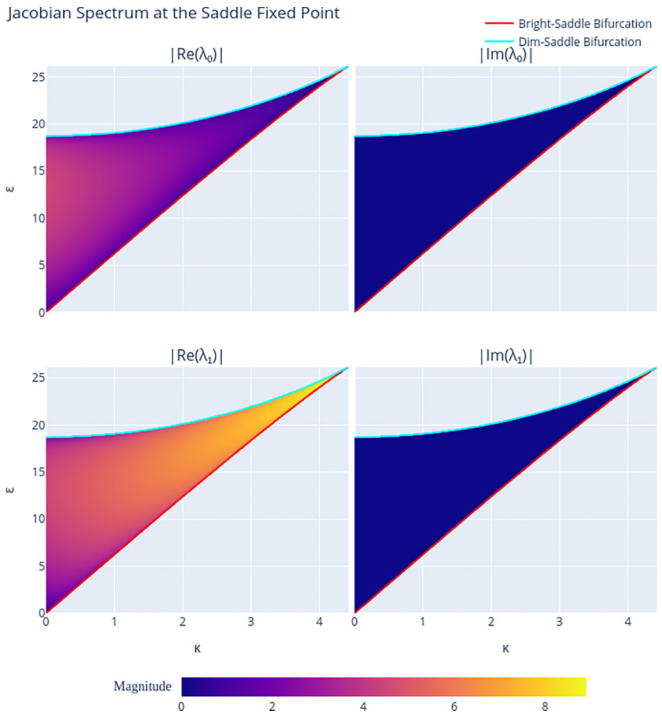

FIG. 6. Eigenvalue spectrum of saddle point. Real and imaginary parts of eigenvalues for the saddle point across parameter space. Unlike the stable fixed points, eigenvalues remain purely real throughout the bistable regime, with characteristic opposite-sign pairs confirming the unstable nature. One eigenvalue approaches zero near bifurcations, indicating soft-mode emergence.

This poses a significant challenge when attempting to find escape trajectories. The eigenvectors of the Jacobian which allow escape are part of the same quadruplet as ingoing eigenvectors which control decaying motion. Just as the decaying path has significant spiralling motion with slow relaxation to the fixed point, the escaping trajectories will have significant spiralling motion with slow escape rates. The widely differing timescales and accumulation of numerical errors make it challenging to find the exact path from the fixed point to the saddle point.

In the top-right panel we examine the system close to the cusp point where the bistable regime closes ($\kappa/\delta = 4.3/7.8$, $\epsilon/\delta = 25.6/7.8$). The motion is quite different: the dim fixed point becomes a node and the system moves almost linearly from one point to the other, making it much easier to find the exact trajectory.

Figure 7 quantifies the computational challenges by showing how the ratio of imaginary to real eigenvalue parts diverges at small decay rates, making numerical path-finding increasingly difficult due to the separation of timescales between fast oscillatory motion and slow escape dynamics.

The emergence of soft modes near bifurcation points is illustrated in Fig. 8, which shows how one eigenvalue of the saddle point approaches zero as the system approaches the bifurcation. This soft mode represents the critical slowing down of dynamics perpendicular to the approaching bifurcation, providing insight into the mechanism by which the saddle point and stable fixed point merge at the bifurcation boundary.

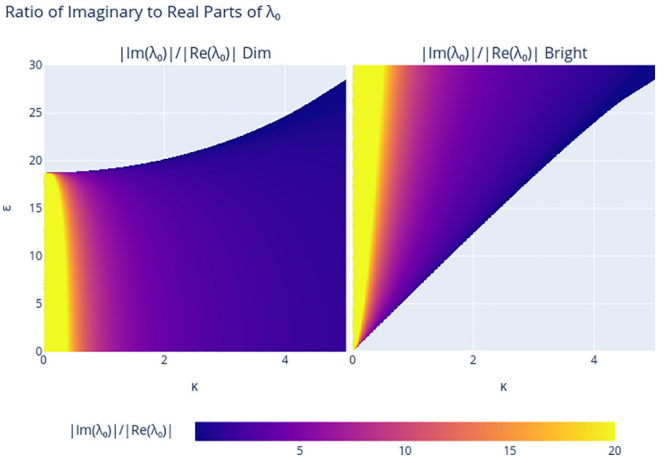

FIG. 7. Parameter regimes for trajectory computation. Ratio of imaginary to real parts of eigenvalues for dim and bright fixed points. The diverging ratio as decay rate approaches zero indicates increasing computational difficulty, which can be mitigated by working close to bifurcation points where the ratio remains finite.

5. Switching path problem formulation

Our objective is to find optimal paths $\mathbf{Z}(t)$ that connect stable fixed points $\mathbf{Z}_0$ (nodes or foci) to the saddle point $\mathbf{Z}_s$. These paths represent the most probable escape trajectories in the four-dimensional phase space and determine the switching rates between metastable states.

The key insight is to use the eigenvector structure of the Jacobian at both fixed points to set appropriate boundary conditions. Small deviations from any fixed point can be expressed in the eigenvector basis, allowing us to control the boundary conditions by specifying which eigenvector directions are active at the start and end of the trajectory.

At each fixed point, the Jacobian possesses both incoming (stable) and outgoing (unstable) eigenvector directions. For a proper switching trajectory, we require that at the initial time the deviation lies purely along eigenvectors leaving the stable point, and at the final time the deviation lies purely along eigenvectors arriving at the saddle point.

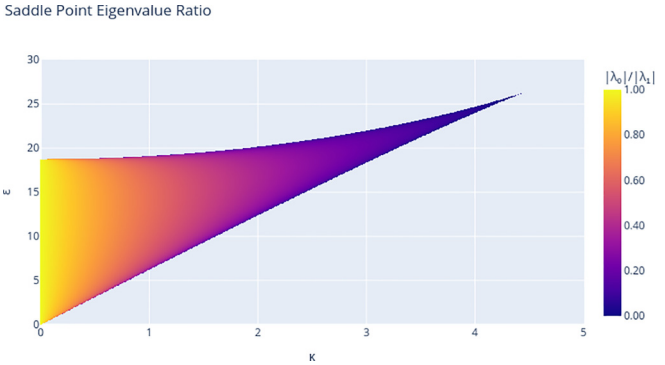

FIG. 8. Soft-mode emergence at saddle point. Ratio of eigenvalues at the saddle point showing the onset of the soft mode. The vanishing of the λ_0 eigenvalue at the bifurcation point indicates the disappearance of the restoring force as the saddle point merges with the stable fixed point, revealing the critical slowing down characteristic of the approach to the bifurcation.

With these paths, we calculate the corresponding action using the simplified form

$$S_{\text{aux}} = -\int dt[\dot{x}_c x_q + \dot{p}_c p_q], \tag{B18}$$

since the Hamiltonian is conservative and the initial and final points lie in the classical plane where $H = 0$.

6. Numerical solution via collocation

To find the switching paths connecting stable fixed points to the saddle point, we formulate a boundary-value problem (BVP) with appropriate boundary conditions derived from our stability analysis and we solve this BVP using a collocation method implemented in SCIPY's `solve_bvp` function [38]. This method expresses the path in terms of cubic splines between a mesh of points known as collocation points. The solver determines the position of the collocation points such that the equations of motion are satisfied to a given tolerance at each point.

The boundary conditions are set using the eigenvector structure at each fixed point to ensure proper asymptotic behavior. This approach transforms the infinite-time problem into a finite-time boundary-value problem while preserving the essential physics.

At the stable fixed point $\mathbf{Z}_0$. At $t \to -\infty$, the trajectory must depart along the unstable manifold. For finite times t_i, we enforce this by requiring that the initial deviation aligns only with unstable eigenvectors:

$$\boldsymbol{L}_i \cdot [\boldsymbol{Z}(t_i) - \mathbf{Z}_0] = 0 \quad \text{for stable modes,} \tag{B19}$$

where $\boldsymbol{L}_i$ are the left eigenvectors corresponding to stable eigenvalues.

At the saddle point $\mathbf{Z}_s$. At $t \to +\infty$, the trajectory must arrive along the stable manifold. For finite times t_f, we enforce this by requiring that the final deviation aligns only with stable eigenvectors:

$$\boldsymbol{L}_j \cdot [\boldsymbol{Z}(t_f) - \mathbf{Z}_s] = 0 \quad \text{for unstable modes,} \tag{B20}$$

where $\boldsymbol{L}_j$ are the left eigenvectors corresponding to unstable eigenvalues.

These projection conditions are implemented using the biorthogonality relationship between left and right eigenvectors. If the right eigenvectors are arranged in matrix R and the corresponding normalized left eigenvectors in matrix L, then any deviation $\Delta\mathbf{Z}$ can be expanded as $\Delta\mathbf{Z} = R\mathbf{c}$, where the coefficients are extracted by $\mathbf{c} = L\Delta\mathbf{Z}$. The boundary conditions then simply require setting specific coefficients to zero.

Two main numerical considerations are important for convergence:

(1) We must use a finite time domain $[t_i, t_f]$ instead of the theoretical $[-\infty, +\infty]$, but the domain should be long enough to ensure the initial and final states are close to the fixed points.

(2) The error tolerance in the collocation method controls the accuracy of the solution, with lower tolerances requiring more collocation points.

(3) An initial guess must be provided for the path between the fixed points. Convergence of the solution is dependent on the quality of this initial guess.

Convergence is verified by checking that the calculated action stabilizes with respect to changes in the time domain and error tolerance. For the calculations in this paper we used $(t_f - t_i)/\delta = 1.28$, a maximum number of 1×10^6 collocation points, and the default error tolerance of 1×10^{-3} at each collocation point.

The collocation method also requires an initial guess. We typically use linear interpolation between the fixed points, which works well near saddle-node bifurcations where the fixed points are close. For more complex paths deeper in the bistable regime, we employ numerical continuation, using solutions from nearby points in parameter space as initial guesses.

Once we obtain the switching path $\boldsymbol{Z}(t)$, we can finally calculate the action, which determines the switching rate between the metastable states, with lower action corresponding to more probable transitions.

The computational implementation of these methods is available as open-source Python code, providing a practical framework for applying the instanton approach to the driven-dissipative system considered in this paper [37].

7. Validation and results

The switching path methodology has been extensively validated through comparison with analytical predictions and numerical simulations. We have computed switching paths and their corresponding actions across different parameter regimes, with particular focus on two key scenarios.

Systematic studies as functions of both κ (at fixed $\epsilon/\delta = 2.44$) and ϵ (at fixed $\kappa/\delta = 0.240$) demonstrate the method's robustness across the bistable regime. The switching paths were computed using boundary-condition thresholds of 10^{-3} to 10^{-2} for proper manifold alignment, with numerical integration performed over finite time domains of $(t_f - t_i)\delta = 78.0$ to 85.8.

Figure 9 shows the results for switching paths and actions as a function of κ at fixed $\epsilon/\delta = 2.44$. The upper panel displays the bifurcation structure with the red and blue lines representing the unstable-bright and unstable-dim bifurcation boundaries, respectively. The lower panel shows the calculated actions for both switching directions: red line for the bright-to-unstable transition $R_{b\to u}$ and blue line for the dim-to-unstable transition $R_{d\to u}$, alongside the analytical Kramers predictions (dashed lines).

Similarly, Fig. 10 presents results for the complementary parameter sweep as a function of ϵ at fixed $\kappa/\delta = 0.240$. The structure mirrors the κ sweep but with the parameter cut oriented vertically in the bifurcation diagram.

8. Comparison with Kramers theory

Close to bifurcation points, our numerically computed Keldysh actions show excellent agreement with analytical Kramers predictions, validating the numerical approach in the regime where one-dimensional approximations are valid. The actions are measured relative to the scaled Planck constant $\lambda = \chi/\delta$. Deeper into the bistable regime, the methods diverge, indicating the breakdown of the one-dimensional (1D) approximation and demonstrating the necessity of the full four-dimensional treatment.

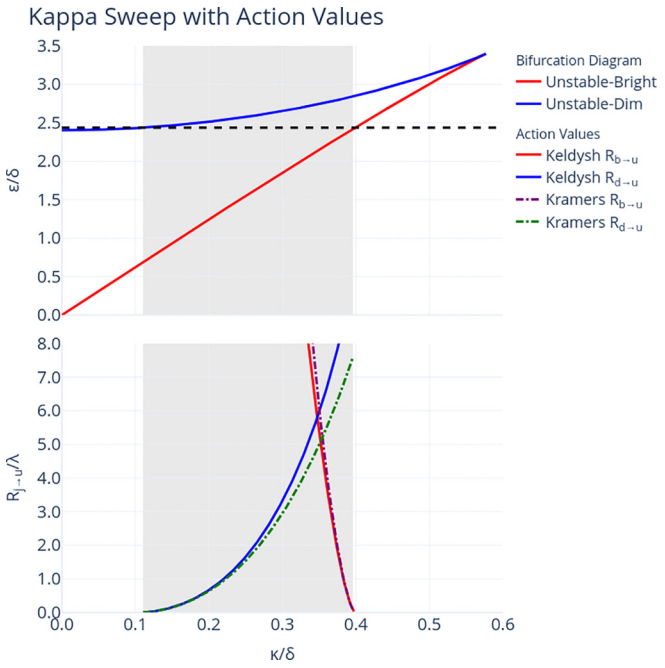

FIG. 9. Switching paths and actions vs κ. Parameter sweep at fixed $\epsilon/\delta = 2.44$ showing (upper panel) the bifurcation structure and (lower panel) the calculated Keldysh actions $R_{b\to u}$ (red) and $R_{d\to u}$ (blue) compared with analytical Kramers predictions (dashed lines). Actions are measured relative to $\lambda = \chi/\delta$. Close agreement near bifurcation points validates the numerical approach, while divergence deeper in the bistable regime indicates breakdown of the one-dimensional approximation.

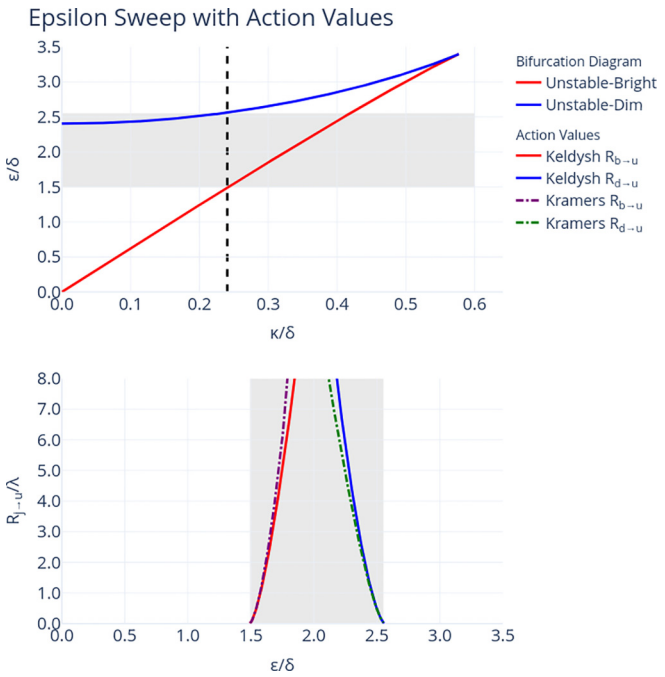

FIG. 10. Switching paths and actions vs ϵ. Parameter sweep at fixed $\kappa/\delta = 0.240$ showing (upper panel) the bifurcation structure and (lower panel) the calculated Keldysh actions compared with analytical Kramers predictions. The agreement validates the numerical approach close to bifurcation points, while convergence challenges in the middle of the bistable regime prevent action calculation in that region.

9. Computational challenges

The method's effectiveness depends on the parameter regime. Near saddle-node bifurcations, where fixed points are close and soft modes emerge, linear interpolation provides adequate initial guesses and convergence is readily achieved. However, at small decay rates deep in the bistable regime, where stable fixed points exhibit strong oscillatory behavior, numerical continuation from neighboring parameter points becomes essential for obtaining converged solutions. In the middle of the bistable regime for the ϵ sweep, convergence was not achieved, highlighting these computational limitations.

The complete computational framework, including parameter sweep generation, path calculation, and action evaluation, is available in the open-source metastable Python package [37], providing a practical toolkit for applying the instanton approach to driven-dissipative quantum systems.

APPENDIX C: EXTRACTING BRIGHT AND DIM STATES FROM LIOUVILLIAN EIGENVECTORS

In the following we show how the relaxation rate γ_{total} and stationary probabilities $p^{ss}_{\text{b(d)}}$ can be calculated by studying the Lindblad master equation directly. The eigenvalues and eigenvectors of the Liouvillian matrix were found using the Lanczos eigensolver available in SCIPY [38]. This provides an alternative method for calculating the switching rates which can then be compared with the results of the Keldysh formalism. The master equation in question is given by

$$\partial_t \rho = -i[H, \rho] + \kappa(a\rho a^\dagger - a^\dagger a\rho - \rho a^\dagger a). \tag{C1}$$

Since the master equation is linear, we can rewrite the evolution in terms of the Liouvillian superoperator $\mathcal{L}$ [39],

$$\partial_t \rho = \mathcal{L}\rho. \tag{C2}$$

The eigenvalue equation of this operator takes the form $\mathcal{L}\rho_m = -(\gamma_m + i\omega_m)\rho_m$, where the real and imaginary components of the complex eigenvalues are denoted by γ_m and ω_m, respectively. We can write down the evolution of a state in this eigenbasis as

$$\rho(t) = \sum_m c_m e^{-(\gamma_m + i\omega_m)t}\rho_m. \tag{C3}$$

We see that γ_m represents the decay rate of the component ρ_m and ω_m represents its oscillation frequency. It is known that $\gamma_m \geqslant 0$ for all eigenvectors [39] and this ensures that ρ is well behaved at long times. States for which $\gamma_m > 0$ will decay over time until the only remaining components of $\rho(t)$ consists of those eigenvectors for which $\gamma_m = 0$. For our system we expect a single such eigenvector which forms the steady state, denoted ρ_{ss}. In the bistable regime this state will consist of a mixture of the two metastable states, as we can see in the Wigner function displayed in Figs. 1(a) and 1(b) and in the trajectory displayed in Figs. 2(a) and 2(b):

$$\rho_{\text{ss}} = p_{\text{b}}\rho_{\text{b}} + p_{\text{d}}\rho_{\text{d}}. \tag{C4}$$

However, we are also interested in the asymptotically decaying eigenvector, i.e., the eigenvector with the smallest finite value of γ_m, which will be denoted ρ_{ad}. At long times the

state of the system will consists of a mixture of the steady-state and this asymptotically decaying eigenvector, all other eigenvectors having already decayed to negligible levels.

We now have two alternative descriptions of the transient response of the system: one from the Keldysh approach and one from the Liouvillian approach. The Keldysh approach shows us that the system approaches steady-state via switching events between the two metastable states which eventually cause the system to reach a dynamic equilibrium whereby the rates in each direction are balanced. This equilibration occurs at the rate described in Eq. (14). But now we see that this process is also described by the decay of an unknown asymptotically decaying eigenvector at rate $\gamma_{\rm ad}$. These rates are in fact identical, i.e., $\gamma_{\rm ad} = \gamma_{\rm total}$.

Furthermore, in our two-state approximation we can show that the asymptotically decaying state is proportional to the difference between the bright and dim states $\rho_{\rm ad} \propto \rho_{\rm d} - \rho_{\rm b}$. The argument is as follows: In the two-state approximation we can write the asymptotically decaying state as

$$\rho_{\rm ad} = N_{\rm d}\rho_{\rm d} + N_{\rm b}\rho_{\rm b}, \tag{C5}$$

where $N_{\rm d}$ and $N_{\rm b}$ are constants that will be determined below. Meanwhile, at long times we can rewrite Eq. (C4) as

$$\rho(t) = \rho_{\rm ss} + c_{\rm ad}\rho_{\rm ad}e^{-\gamma_{\rm ad}t}. \tag{C6}$$

Since $\rho_{\rm d}$, $\rho_{\rm b}$, $\rho(t)$, and $\rho_{\rm ss}$ are all physical states their traces are all equal to 1. Applying this above we find

$$\mathrm{Tr}[\rho(t)] = \mathrm{Tr}(\rho_{\rm ss}) + c_{\rm ad}\mathrm{Tr}(\rho_{\rm ad})e^{-\gamma_{\rm ad}t}, \tag{C7}$$

$$1 = 1 + c_{\rm ad}\mathrm{Tr}(\rho_{\rm ad})e^{-\gamma_{\rm ad}t}. \tag{C8}$$

This can only be satisfied in general if $\mathrm{Tr}(\rho_{\rm ad}) = 0$ and hence we must have $N_{\rm d} = -N_{\rm b}$. Hence the asymptotically decaying state can be written as

$$\rho_{\rm ad} = N(\rho_{\rm d} - \rho_{\rm b}), \tag{C9}$$

where the normalization factor $N = N_{\rm d} = -N_{\rm b}$.

Given that the steady and asymptotically decaying eigenvectors are linearly independent mixtures of bright and dim states, we might consider how we can combine them to isolate their components and the corresponding occupation probabilities. These could then be used to calculate the switching rates in Eq. (14).

In Fig. 11 we illustrate the method of extracting the bright and dim states from the eigenstates of the Liouvillian superoperator describing the evolution of the state at $(\chi/\kappa, \delta/\kappa, \epsilon/\kappa) = (1.0, 6.0, 3.6)$. We first display the Wigner functions of the steady state ρ_{ss} [Fig. 11(a)] and the asymptotically decaying eigenvector $\rho_{\rm ad}$ [Fig. 11(b)] and we observe that these components both consist of a weighted sum of bright and dim states according to the structure outlined in Eqs. (C4) and (C9). In the steady state the weights correspond to probabilities and are both positive, resulting in the two peaks observed in Fig. 11(a). Meanwhile in the asymptotically decaying eigenvector the weights are equal in magnitude but opposite in sign, which results in the peak and dip seen in Fig. 11(b).

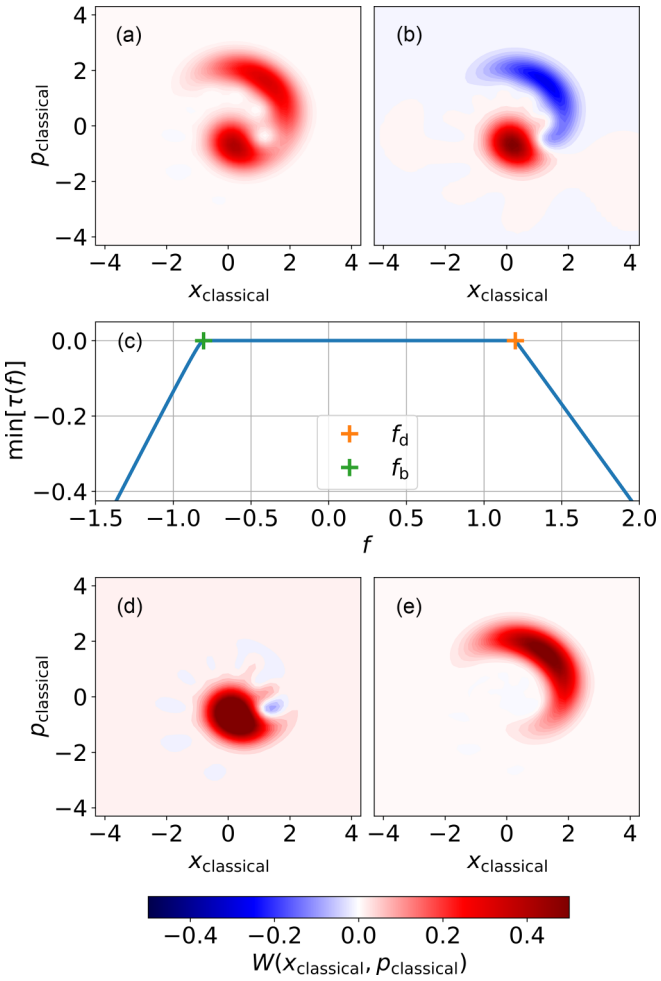

FIG. 11. Extracting the metastable states from the Liouvillian. Wigner functions of the steady state [panels (a)] and the asymptotically decaying eigenvector [panels (b)] produced at $(\chi/\kappa, \delta/\kappa, \epsilon/\kappa) = (1.0, 6.0, 3.6)$. The steady state is a mixture of the two metastable states while the asymptotically decaying eigenvector is an antisymmetric mixture. This allows us to reconstruct the metastable states from a sum of steady and asymptotically decaying eigenvectors. (c) The smallest eigenvalue of $\tau(f) = \rho_{\rm ss} + f\rho_{\rm ad}$. At $f = f_{\rm b}$ and $f = f_{\rm d}$ the state $\tau(f)$ consists entirely of the (d) dim and (e) bright states, respectively.

These two states can be combined to form the mixture τ defined by

$$\begin{aligned}\tau(f) &= \rho_{\rm ss} + f\rho_{\rm ad} \\ &= (p_{\rm b} - fN)\rho_{\rm b} + (p_{\rm d} + fN)\rho_{\rm d}.\end{aligned} \tag{C10}$$

To extract the bright and dim states we plot the minimum eigenvalue $\min(\tau)$ against f in Fig. 11(c) and identify the points at which this eigenvalue falls below zero. Finally, we plot the Wigner functions of the resulting bright and dim states. In Fig. 11(d) we display $\rho_{\rm d} \propto \tau(f_{\rm d})$ while in Fig. 11(e) we display $\rho_{\rm b} \propto \tau(f_{\rm b})$. We see that these states consist of a single peak, as expected.

In order that $\rho_{\rm b}$ and $\rho_{\rm d}$ are both physically realistic states they should be positive semidefinite, i.e., they should have no negative eigenvalues. If we define the function $\min(\tau)$, which returns the smallest eigenvalue of τ, then our condition can

now be stated as $\min(\rho_b),\ \min(\rho_d) \geqslant 0$. Next we assume the metastable states do not overlap, i.e., $\mathrm{Tr}(\rho_b \rho_d) = 0$, which is a good approximation provided the drive amplitude is sufficiently strong for the bistable states to be well separated. Given this assumption, the state $\tau(f)$ will be positive semidefinite if and only if the coefficients of the bistable states are both greater than or equal to zero. Therefore, we can identify the values $f_d = p_b/N$ and $f_b = -p_d/N$ by plotting $\min[\tau(f)]$ as a function of f and locating where this function falls below zero. The values of f_b and f_d thus obtained are then combined with the normalization $p_b + p_d = 1$ to obtain the occupation probabilities

$$p_b = \frac{f_b}{f_b - f_d}, \quad p_d = -\frac{f_d}{f_b - f_d}, \tag{C11}$$

which are plotted in Fig. 2(c).

APPENDIX D: SCALING OF THE BARRIER HEIGHT

Close to saddle-node bifurcation points, switching between metastable states can be expressed as a one-dimensional Kramers problem [13]. The barrier height for escape from a metastable state is quantified by the quantum activation energy, R_A, given by

$$R_A = \frac{\sqrt{2}|\eta|^{3/2}}{3D_B|b|^{1/2}\beta_B^{3/4}}. \tag{D1}$$

This expression involves four key quantities: η, D_B, b, and β_B. In the following, we summarize the parameter definitions and relationships from Ref. [13] and explain how these parameters are related to the variables used in the body of this paper: κ, δ, χ, and ϵ.

1. Distance from bifurcation

The parameter η measures the distance from the bifurcation point and is defined as

$$\eta = \beta - \beta_B, \tag{D2}$$

where β is a dimensionless measure of the drive strength and β_B denotes the bifurcation value of β. In our analysis, η indicates how far the system is from the critical point at which the metastable state vanishes.

2. Driving strength

The drive intensity parameter β is obtained via

$$\beta = \frac{2\lambda\epsilon^2}{\delta^2}, \tag{D3}$$

where

(1) λ is the effective (rescaled) Planck constant,
(2) ϵ is the amplitude of the drive, and
(3) δ is the detuning.

3. Scaled Planck Constant

The effective Planck constant is given by

$$\lambda = \frac{\chi}{|\delta|}, \tag{D4}$$

where χ is the nonlinearity of the oscillator. In our analysis, λ quantifies the magnitude of quantum fluctuations and is assumed to be small in the semiclassical regime.

4. Diffusion coefficient

The diffusion coefficient D_B, which characterizes the noise-induced diffusion of the slow variable near the bifurcation, is given by

$$D_B = \frac{1}{2\Omega}, \tag{D5}$$

under the assumptions of zero thermal occupation and negligible dephasing. Here, Ω sets the scale of the system dynamics. The parameter Ω is defined as

$$\Omega = \frac{|\delta|}{\kappa}, \tag{D6}$$

where

(1) $|\delta|$ is the magnitude of the detuning, and
(2) κ is the damping rate.

5. Bifurcation threshold

The quantity β_B represents the bifurcation point, i.e., the critical value of β at which a metastable state merges with a saddle point. In our analysis, two bifurcation thresholds emerge (denoted β_1 and β_2). They are expressed in terms of Ω as

$$\beta_{(1,2)B} = \frac{2}{27}\left[1 + \frac{9}{\Omega^2} \mp \left(1 - \frac{3}{\Omega^2}\right)^{3/2}\right], \tag{D7}$$

where the upper $(-)$ and lower $(+)$ signs correspond to the different branches of the bifurcation diagram.

6. Curvature parameter and its calculation

The parameter b, which encodes the local curvature of the effective potential near the bifurcation, is given by

$$b = -\beta_B^{1/2}\frac{1}{2Y_B}[1 - 2\Omega^2 Y_B + \Omega^2]. \tag{D8}$$

The quantity Y_B is expressed in terms of Ω as

$$Y_B = \frac{1}{3}\left[2 \pm \sqrt{1 - \frac{3}{\Omega^2}}\right], \tag{D9}$$

where the choice of sign depends on the particular bifurcation branch under consideration.

[1] M. I. Dykman and V. N. Smelyanskii, Zh. Eksp. Teor. Fiz. **94**, 61 (1988) [Sov. Phys. JETP **67**, 1769 (1988)].
[2] M. Marthaler and M. I. Dykman, Phys. Rev. A **73**, 042108 (2006).
[3] S. Ghashghaie, W. Breymann, J. Peinke, P. Talkner, and Y. Dodge, Nature (London) **381**, 767 (1996).
[4] L. Knopoff and Y. Kagan, J. Geophys. Res. **82**, 5647 (1977).

[5] R. Vijay, M. H. Devoret, and I. Siddiqi, Rev. Sci. Instrum. **80**, 111101 (2009).

[6] K. Lehnertz, *Extreme Events in Nature and Society* (Springer, Berlin, Heidelberg, 2006), pp. 123–143.

[7] A. Kamenev and B. Meerson, Phys. Rev. E **77**, 061107 (2008).

[8] T. Wilhelm, BMC Syst. Biol. **3**, 90 (2009).

[9] A. Taitelbaum, R. West, M. Assaf, and M. Mobilia, Phys. Rev. Lett. **125**, 048105 (2020).

[10] F. Thompson and A. Kamenev, Phys. Rev. Res. **4**, 023020 (2022).

[11] H. Kleinert, *Path Integrals in Quantum Mechanics, Statistics, Polymer Physics, and Financial Markets*, 5th ed. (World Scientific, Singapore, 2009).

[12] B. Caroli, C. Caroli, and B. Roulet, J. Stat. Phys. **26**, 83 (1981).

[13] M. I. Dykman, Phys. Rev. E **75**, 011101 (2007).

[14] M. Dykman, *Fluctuating Nonlinear Oscillators: From Nano-Mechanics to Quantum Superconducting Circuits* (Oxford University Press, Oxford, 2012).

[15] T. K. Mavrogordatos, G. Tancredi, M. Elliott, M. J. Peterer, A. Patterson, J. Rahamim, P. J. Leek, E. Ginossar, and M. H. Szymańska, Phys. Rev. Lett. **118**, 040402 (2017).

[16] P. Brookes, G. Tancredi, A. D. Patterson, J. Rahamim, M. Esposito, T. K. Mavrogordatos, P. J. Leek, E. Ginossar, and M. H. Szymanska, Sci. Adv. **7**, eabe9492 (2021).

[17] V. Elgart and A. Kamenev, Phys. Rev. E **70**, 041106 (2004).

[18] A. Kamenev, *Field Theory of Non-Equilibrium Systems* (Cambridge University Press, 2011).

[19] E. G. D. Torre, S. Diehl, M. D. Lukin, S. Sachdev, and P. Strack, Phys. Rev. A **87**, 023831 (2013).

[20] L. M. Sieberer, M. Buchhold, and S. Diehl, Rep. Prog. Phys. **79**, 096001 (2016).

[21] W. H. Miller, J. Chem. Phys. **62**, 1899 (1975).

[22] P. Hänggi, P. Talkner, and M. Borkovec, Rev. Mod. Phys. **62**, 251 (1990).

[23] P. G. Wolynes, J. Chem. Phys. **87**, 6559 (1987).

[24] J. Cao, C. Minichino, and G. A. Voth, J. Chem. Phys. **103**, 1391 (1995).

[25] P. D. Drummond and D. F. Walls, J. Phys. A: Math. Gen. **13**, 725 (1980).

[26] M. Elliott and E. Ginossar, Phys. Rev. A **94**, 043840 (2016).

[27] L. S. Bishop, E. Ginossar, and S. M. Girvin, Phys. Rev. Lett. **105**, 100505 (2010).

[28] M. Elliott, J. Joo, and E. Ginossar, New J. Phys. **20**, 023037 (2018).

[29] K. W. Murch, E. Ginossar, S. J. Weber, R. Vijay, S. M. Girvin, and I. Siddiqi, Phys. Rev. B **86**, 220503(R) (2012).

[30] E. Ginossar, L. S. Bishop, D. I. Schuster, and S. M. Girvin, Phys. Rev. A **82**, 022335 (2010).

[31] M. H. Szymańska, J. Keeling, and P. B. Littlewood, Phys. Rev. B **75**, 195331 (2007).

[32] A. N. Jordan and E. V. Sukhorukov, Phys. Rev. Lett. **93**, 260604 (2004).

[33] D. M. Roma, R. A. O'Flanagan, A. E. Ruckenstein, A. M. Sengupta, and R. Mukhopadhyay, Phys. Rev. E **71**, 011902 (2005).

[34] H. M. Wiseman and G. J. Milburn, *Quantum Measurement and Control* (Cambridge University Press, New York, 2009).

[35] J. R. Johansson, P. D. Nation, and F. Nori, Comput. Phys. Commun. **183**, 1760 (2012).

[36] V. Peano and M. I. Dykman, New J. Phys. **16**, 015011 (2014).

[37] P. Brookes, Metastable, gitHub repository (2025), https://github.com/paulsbrookes/metastable.

[38] P. Virtanen, R. Gommers, T. E. Oliphant, M. Haberland, T. Reddy, D. Cournapeau, E. Burovski, P. Peterson, W. Weckesser, J. Bright, S. J. van der Walt, M. Brett, J. Wilson, K. J. Millman, N. Mayorov, A. R. J. Nelson, E. Jones, R. Kern, E. Larson, C. J. Carey *et al.*, Nat. Methods 17, 261 (2020).

[39] F. Minganti, A. Biella, N. Bartolo, and C. Ciuti, Phys. Rev. A **98**, 042118 (2018).